electronics

MDPI

Article

Design of a Fast Robotic Total Station Through Ad Hoc Virtual Experiments and Its Digital Twin †

Henrique Simas [1], Raffaele Di Gregorio [2,*] and Roberto Simoni [3]

[1] Raul Guenther Laboratory of Applied Robotics, Department of Mechanical Engineering, Federal University of Santa Catarina, Florianópolis 88040-900, SC, Brazil; henrique.simas@ufsc.br
[2] Laboratory of Mechatronics and Virtual Prototyping (LaMaViP), Department of Engineering, University of Ferrara, Via Saragat, 1, 44100 Ferrara, Italy
[3] Department of Mobility Engineering, Federal University of Santa Catarina, Joinville 89219-600, SC, Brazil; roberto.simoni@ufsc.br
* Correspondence: raffaele.digregorio@unife.it; Tel.: +39-0532-974828
† This article is a revised and expanded version of paper No. 55 entitled "Dynamic Design of a Fast Robotic Total Station Based on Ad-Hoc-Conceived Virtual Experiments Implemented through a Digital Twin", which was presented at "IEEE/ASME MESA 2024—20th International Conference on Mechatronic, Embedded Systems and Applications", Genova, Italy, 2–4 September 2024.

Abstract: The dynamic performances of an innovative robotic total station (RTS) are assessed while tracking a moving target; also, the results of these performance evaluations are exploited to design its control system. The proposed methodology is novel and uses ad hoc virtual experiments implemented on the digital twin of the studied RTS. This methodology is general and is also applicable for the design of other mechatronic systems. The proposed ad hoc virtual experiments constitute a benchmark for assessing the tracking performances of pointing systems. The application of this methodology to the studied RTS will help complete the RTS's design by determining the most suitable actuators and the control system constants necessary to obtain the assigned dynamic performances. A 3D-printed prototype of the designed RTS was built and is shown in this paper.

Keywords: robotic total station; control system design; digital twin; tracking task

Citation: Simas, H.; Di Gregorio, R.; Simoni, R. Design of a Fast Robotic Total Station Through Ad Hoc Virtual Experiments and Its Digital Twin. *Electronics* **2024**, *13*, 4248. https://doi.org/10.3390/electronics13214248

Academic Editor: Andrea Bonci

Received: 14 September 2024
Revised: 24 October 2024
Accepted: 28 October 2024
Published: 30 October 2024

1. Introduction

Robotic total stations (RTSs) [1] are fully automated pointing systems that point the axis of a telescope toward a target (usually equipped with a reflector) and autonomously measure the local coordinates of the target in polar coordinates. They can also track a moving target and determine its path in the same coordinate system [2,3]. RTSs are widely used in surveying for building maps.

RTSs' functioning principle is simple (see Figure 1a). The telescope axis passes through the center of a universal (U) joint (i.e., the intersection of the two dash-dot lines in Figure 1a). A levelling operation identifies a horizontal plane that passes through the center of the above-said U joint, is perpendicular to the axis (vertical axis) of the first revolute (R) pair of the U joint, and contains the axis (horizontal axis) of the second R pair of the same U joint. Then, by measuring the two rotation angles of the two mutually perpendicular R pairs of the U joint, the pointing direction of the telescope is identified and a laser rangefinder is used to measure the distance of the target from the center of the U joint. The rotation around the vertical axis (φ in Figure 1a) is named the pan rotation and the rotation around the horizontal axis (ζ in Figure 1a) is named the tilt rotation.

The tracking ability of RTSs has been recently exploited for monitoring civil structures [4–11] with the aim of measuring the time histories of their small displacements in response to dynamic loads and their natural frequencies. In particular, they have been employed either together with other instruments or alone to measure the natural frequencies of different types of bridges excited by the transit of people or vehicles, that is, when

the oscillation amplitude has the order of centimeters and the oscillation frequency is lower than 1 Hz. In civil structures, the frequency border of 1 Hz is sufficient for many applications; nevertheless, extending this border up to 5 Hz, or better, to 10 Hz, would greatly extend this field of application. Unfortunately, in these applications, RTSs have good performances when the oscillation frequencies are lower than 3 Hz (see Ref. [12] for details).

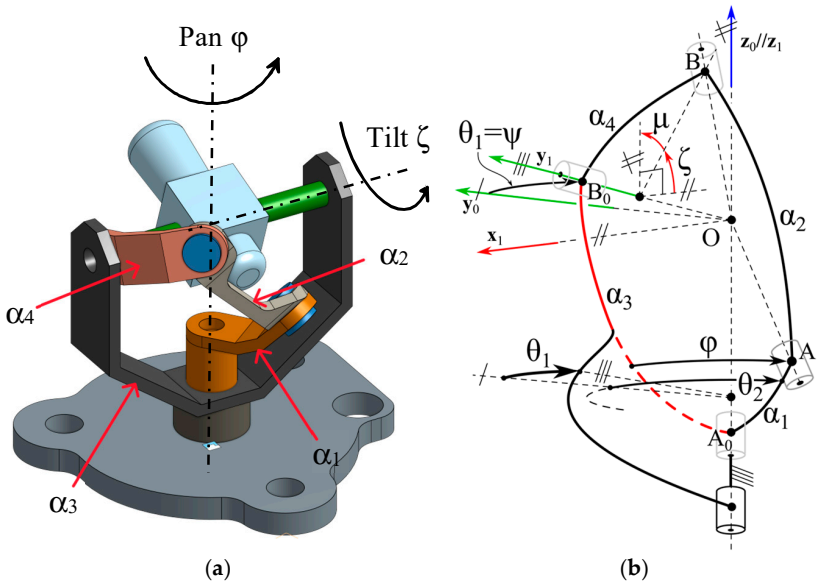

Figure 1. CAD model (**a**) and kinematic scheme (**b**) of the RTS architecture identified in [13] (reproduced from [13]).

Reducing mobile masses is a viable design technique for extending the tracking frequency bandwidth of an RTS. Indeed, commercial RTSs typically weigh between 5 kg and 9.5 kg (see Table 1 of Ref. [13]) and this weight is mainly loaded on their mobile parts, whereas the telescope, which is the only part to move, weighs more or less 0.5 kg. Moving the electrically supplied parts (e.g., actuators, Wi-Fi antennas, displays, etc.) together with their batteries onto the RTS frame (base) is a design strategy that can greatly reduce the mobile masses. Most of these components (e.g., Wi-Fi antennas, onboard computers, and displays) are moveable onto the base without changing the architecture of the mechanism that moves the telescope. However, moving the actuators onto the base requires this architecture is changed from serial to parallel. Serial architectures are open kinematic chains (in this case, the U joint) that connect the base to the end effector (in this case, the link carrying the telescope), whereas parallel architectures feature at least two kinematic chains (limbs) that simultaneously connect the end effector to the base. In general, parallel architectures are stiffer and more precise than their serial counterparts, which are appealing features for a measurement system. Parallel architectures that orientate a line with respect to their base are named parallel pointing systems (PPSs).

In a previous paper [13], the authors reviewed the literature on the type synthesis of PPS architectures (e.g., [14–16]) and selected the most suitable ones for RTSs. Then, they proceeded to a dimensional synthesis and accuracy analysis of the selected PPS architectures and, by comparing the obtained results, concluded that the most promising PPS architecture for RTSs is a particular spherical five-bar linkage (Figure 1) with the first and the fifth R pair axes coinciding with one another.

In this paper, the dynamic performances of this particular spherical five-bar linkage are considered and the design of the innovative RTS architecture is completed by sizing the control system together with the choice of the actuation system. The methodology adopted for this design process is based on ad hoc virtual experiments that are implemented on the digital twin of the RTS architecture. The presented design method is also applicable to

other mechatronic systems and the proposed virtual experiments can be a benchmark for evaluating the tracking performances of pointing systems.

The paper is organized as follows. Section 2 provides the necessary background concepts and presents the adopted methodology together with the ad hoc virtual experiments. Section 3 illustrates the results of the application of the proposed design methodology to the innovative RTS architecture. Then, Section 4 discusses the obtained results and Section 5 draws the conclusions.

2. Materials and Methods

Figure 1a shows the 3D CAD model of the RTS based on the particular spherical 5-bar RTS architecture identified in [13]. With reference to Figure 1a, φ (pan angle) and ζ (tilt angle) denote the rotation angles of the two mutually orthogonal R pairs that constitute the U joint and guide the direction of the telescope axis. A motor mounted on the RTS base directly controls the pan rotation, which is around the vertical axis. In contrast, the tilt rotation is actuated through a spherical kinematic chain of type RRR with the spherical motion center coincident with the U joint center and the R pair adjacent to the base that is actuated and that has the axis coincident with the vertical axis.

Figure 1b shows the kinematic scheme of the same RTS. With reference to Figure 1b, O is the center of the U joint and the angles α_i, in which i = 1, . . .,4, are geometric constants of the binary links connecting two adjacent R pairs. The dimensional synthesis illustrated in [13] has led the authors to determine the following values for the geometric constants: $\alpha_1 = 46.7805^\circ = 0.81647$ rad, $\alpha_2 = \alpha_3 = 90^\circ = \pi/2$ rad, and $\alpha_4 = 57.29578^\circ = 1$ rad.

All these design choices allow the telescope to perform a complete pan rotation while the tilt angle can independently range from $\zeta_{min} = -20^\circ$ to $\zeta_{max} = \zeta_{min} + 120^\circ = 100^\circ$ in which tilt's phase reference is the horizontal plane (see Figure 1b).

Once the geometric constants of the kinematic scheme have been determined, the actual realization of a mechatronic system requires the sequential implementation of the following steps: (a) definition of the actual geometry of the links through technical drawings, (b) design of the control system, and (c) validation of the project. Step (a) takes into account the loads applied to the links and the need to avoid interference of links during motion to define the actual geometry of the links. Step (b) takes into account the machine tasks and the requested performances to define the architecture of the control system. Step (c) checks that the design requirements are met through suitable tests. These steps will be implemented through the following procedure:

(i) The digital twin of the RTS is built starting from its CAD model;
(ii) The architecture of the control system is defined and the parameters of the chosen control system architectures are identified;
(iii) Ad hoc virtual experiments are devised firstly to tune the parameters of the control system and then to evaluate the performances of the designed mechatronic system.

2.1. Digital Twin

The CAD model shown in Figure 1a was built with the CAD software Onshape (used online at (last accessed on 10 September 2024): https://www.onshape.com/en/education/sign-up). Inside Onshape, in order to transform the geometric model into a physical model to use in a simulation environment, Aluminum 5052, with density of 3 g/cm^3, was chosen as material for all of the mechanical parts. Such a material is commonly used for light components of devices like an RTS. Moreover, the geometry of the telescope (Figure 2) has been adjusted so that its center of mass coincides with the U joint center (i.e., it is balanced) and that its weight, equal to 0.504 kg, and its mass moments of inertia (Figure 2) are comparable to those encountered in commercial RTSs.

The CAD model of a machine, even when integrated with mass distribution data, takes into account only the mechanical skeleton of the mechatronic system. Such a model, to become a "digital twin" of the real system, must be imported into a multiphysics environment in which the other parts (e.g., the controller) of the system can also be modeled

and are able to interact with it. Accordingly, after having transformed the geometric model into a physical model, it was imported into the multibody simulation environment Matlab Simscape [17,18] (version R2023b), which is a toolbox of the multiphysics simulation environment Matlab Simulink.

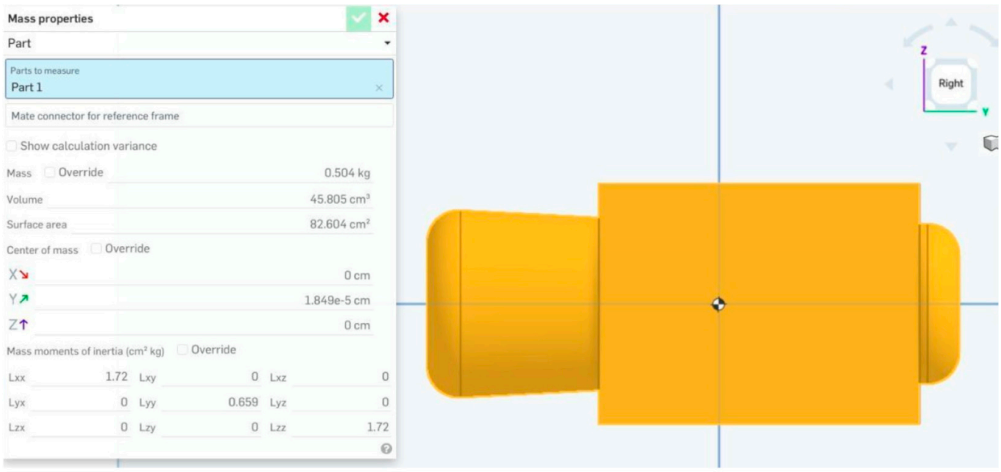

Figure 2. Model of the telescope and mass distribution data (center of mass and mass moments of inertia).

Figure 3 shows the studied RTS imported into Matlab Simscape. Figure 3a presents the block diagram detailing each component (link) of the RTS, along with its interconnections through revolute joints. Meanwhile, Figure 3b displays the multibody model within Matlab Simscape ready to be used in any virtual experiment. Matlab Simscape allows us to set up several parameters of this digital twin, including the friction in the R pairs. This parameter was set to 0.01 Nm.

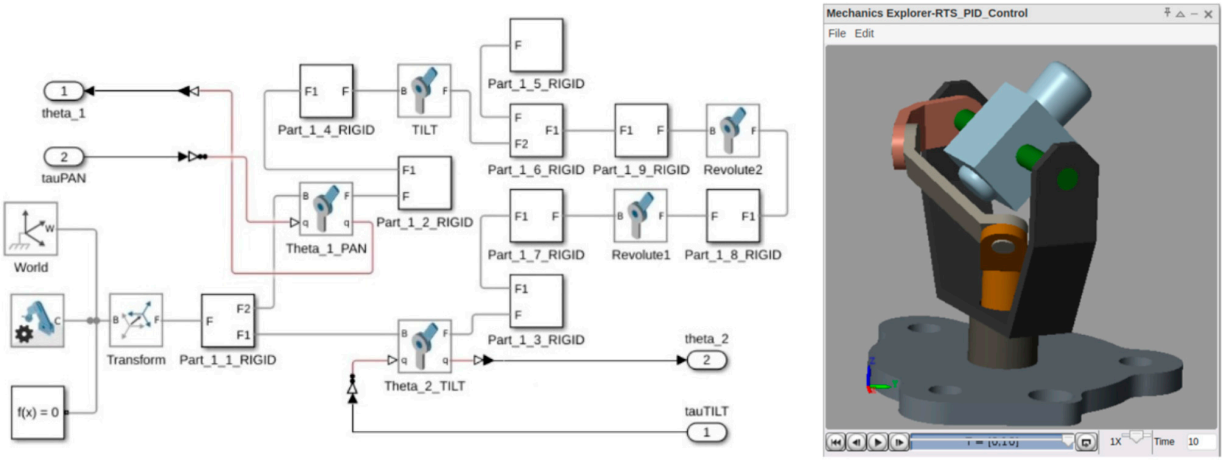

(**a**) (**b**)

Figure 3. Multibody model of the RTS: (**a**) Block diagram of the CAD model imported in Matlab® Simscape and (**b**) CAD parts assembled in Matlab® Simscape.

2.2. Design of the Control System

Ample studies in the literature exist on proportional–integral–derivative (PID) controllers (see [19–21], for instance). Also, PID controllers are by far the most adopted for industrial and robotic applications [22,23] as, in general, they are cheaper, easier to tune [24–26], and can quickly counter disturbances with minimal overshoot during setpoint tracking. Moreover, Matlab Simulink provides a number of commands to insert and tune

PID controllers. All these considerations led the authors to choose a two-degree-of-freedom (2-DOF) PID controller as type of controller for the present project.

With reference to such a controller, in the present project, the relationship between controller's output, U(s), where "s" is the complex variable of the Laplace transform, and its two inputs, which are the desired reference value, r(s), and the plant output value, y(s), is modeled with the following standard parallel form [19–21]:

$$U(s) = [K_p + \frac{K_i}{s} + \frac{K_d s}{T_f s + 1}]E(s) \quad (1)$$

where $E(s) = r(s) - y(s)$ is the error function, K_p is the proportional gain, K_i is the integration gain, K_d is the derivative gain, and T_f is the derivative filter time. K_p, K_i, K_d, and T_f are the controller parameters that must be tuned to allow the RTS to be able to track a target up to at least 10 Hz. The chosen tuning procedure is a trial-and-error procedure based on the below-defined virtual experiments.

Figure 4 shows the block diagram of the complete mechatronic system. With reference to Figure 4, the action of the control system can be summarized as follows. Target's actual coordinates are transformed into "desired" actuated joint variable values through the "inverse-kinematics" block. The two 2-DOF PID controllers receive the actual actuated joint variables together with their desired values as input and produce the command signals that enter into the blocks that model two DC motors, which actuate the system. The outputs of the DC motor blocks (Figure 5) enter into the digital twin of the RTS, built in Matlab Simscape, which, by solving for the direct dynamics of the mechanical system, provides, as output, the corresponding values of the actual actuated joint angles (i.e., the angles θ_1 and θ_2 in Figure 1b). These angle values are fed into the "forward-kinematics" block that computes the corresponding values of the actual pan, φ, and tilt, ζ, angles of the telescope axis, which must be compared with their desired values φ_d and ζ_d, which are the pan and tilt angles locating the target.

The algorithms implemented in the inverse and forward kinematics blocks are presented in detail in [13]. Such algorithms use simple closed-form formulas that practically do not introduce computation delays into the controller.

Figure 5 shows the physical model (Figure 5a) and the corresponding block diagram (Figure 5b) of the DC motor used in the simulation. This model is standard for this type of motor. The parameters of this model are L_a, R_a, J, B, K_m, and K_e. The values of these parameters, which are suitable to control the RTS, were determined with the methodology proposed in [21] by taking into account the DC motors available on the market.

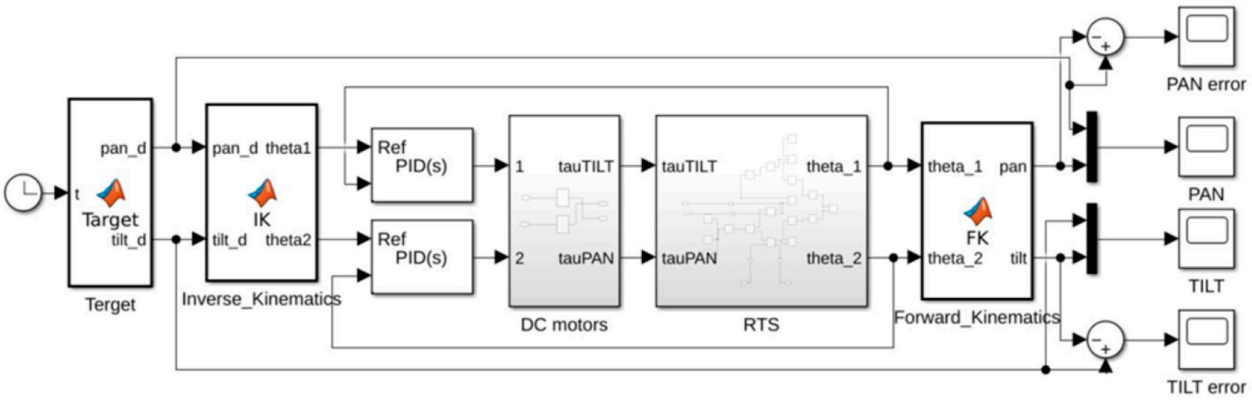

Figure 4. Block diagram of the complete mechatronic system as modeled in Matlab Simulink.

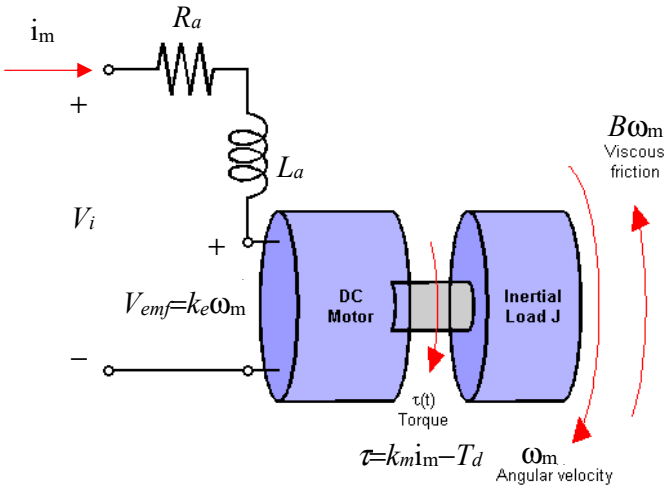

(**a**)

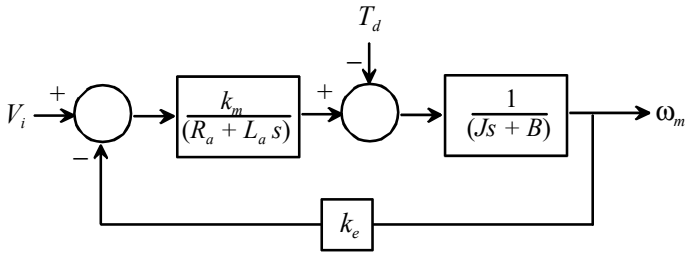

(**b**)

Figure 5. DC motor: (**a**) physical model (T_d is a resistant torque due to disturbances), and (**b**) block diagram used in the simulation.

2.3. Ad Hoc Virtual Experiments

The virtual experiment campaign must be conceived so that, firstly, it determines the parameters of the controller (i.e., K_p, K_i, K_d, and T_f) and of the DC motor (i.e., L_a, R_a, J, B, K_m, and K_e) that can reasonably guarantee a good tracking performance up to 10 Hz, and then, it computes the frequency response of the so-sized system to verify that the requested tracking performances in the frequency range [0, 10] Hz are obtained. Accordingly, the steps to implement are as follows:

(I) Definition of a virtual experiment that allows for the determination of the frequency response of the system at a given frequency;
(II) Assignment of tentative values to the set of parameters to size;
(III) Execution of the virtual experiment, defined in step (I), at a given fixed frequency that could be the most problematic (in our case, this frequency is 10 Hz);
(IV) Evaluation of the results obtained from the experiment implemented in step (III); *if* the result are satisfactory, *then* accept the assigned parameter values as sizes of the system and continue, *else* change the tentative values of the parameters to size and jump to step (III);
(V) A frequency set is obtained by discretizing an ample range of frequencies, which includes [0, 10] Hz; then, for each frequency value of the obtained set, the virtual experiment is repeated on the system, as sized in previous steps, and the results are stored;

(VI) By using the results obtained and stored in step (V), build the frequency response diagrams of the so-sized system in the ample frequency range used in step (V); *if* the diagrams are satisfactory in [0, 10] Hz, *then* stop, *else* change the system's parameters and jump to step (III).

In the following part of this subsection, step (I), which brings to define the experiment to implement at a given frequency, will be detailed; then, in Section 3, the implementation of the remaining steps of the above procedure will be presented together with the determined values of the controller (i.e., K_p, K_i, K_d, and T_f) and of the DC motor parameters (i.e., L_a, R_a, J, B, K_m, and K_e).

Step I: Definition of the Virtual Experiment to Implement at a Given Frequency

In order to evaluate and correct the RTS performances in tracking a target, the frequency response of the complete mechatronic system (Figure 4) must be determined and then adjusted by changing the values of control system's parameters. Since the mechanical system that moves the telescope is a 2-DOF linkage, its frequency response must be determined through a number of experiments at constant excitation frequencies in which the input signal simultaneously excites both RTS degrees of freedom. These virtual experiments, by changing the excitation frequency, will make the determination of the frequency response possible.

Figure 6 shows the proposed virtual experiment at constant excitation frequency. With reference to Figure 6, the virtual experiment was devised as follows. A mobile point, P_c, moves at constant velocity, v, along a circular path, with radius r (= $||\mathbf{p}_c||$) and center at point O_c, and the telescope of the RTS tries to collimate point P_c during its motion. This set up excites both pan and tilt angles at a frequency given by the following formula:

$$f = \frac{\omega}{2\pi} = \frac{v}{2\pi r}, \tag{2}$$

which highlights that the value of f can be changed by simply changing v.

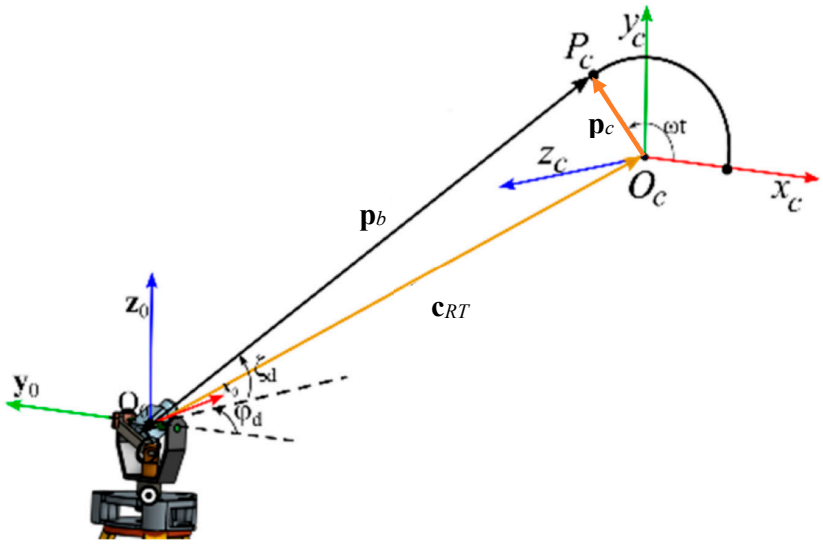

Figure 6. Setup of the ad hoc virtual experiment: the RTS tries to make the telescope axis collimate point P_c which moves along a circular path at constant velocity.

In Figure 6, the Cartesian reference system $O_0x_0y_0z_0$ is fixed to the RTS base and it has origin, O_0, coincident with the U-joint center and z_0-coordinate axis coincident with the vertical axis. The Cartesian reference system $O_cx_cy_cz_c$ is fixed to the circular path of the target point, P_c, and it has origin, O_c, coincident with the center of the circular path and x_cy_c-coordinate plane coincident with the plane of the circular path. The plane of the

circular path is parallel to y_0z_0-coordinate plane and it is located at a given distance from this fixed plane; also, the x_c-coordinate axis is parallel to the y_0-coordinate axis. Therefore, the rotation matrix, ${}^0\mathbf{R}_c$, that transforms vector components measured in $O_cx_cy_cz_c$ into vector components measured in $O_0x_0y_0z_0$ is as follows:

$$ {}^0\mathbf{R}_c = \begin{bmatrix} 0 & 0 & -1 \\ -1 & 0 & 0 \\ 0 & 1 & 0 \end{bmatrix} \tag{3} $$

In $O_cx_cy_cz_c$, the position vector, $\mathbf{p}_c$, of the target point, P_c, is expressed as follows (t is the time):

$$ \mathbf{p}_c = r \begin{pmatrix} \cos \omega t \\ \sin \omega t \\ 0 \end{pmatrix} \tag{4} $$

whereas in $O_0x_0y_0z_0$, the position vector, $\mathbf{p}_\mathrm{b}$, of the same target point is expressed as follows:

$$ \mathbf{p}_b = d_0 \begin{pmatrix} \sin \varphi_d \cos \zeta_d \\ -\cos \varphi_d \cos \zeta_d \\ \sin \zeta_d \end{pmatrix} = \mathbf{c}_{RT} + {}^0\mathbf{R}_c\mathbf{p}_c; \tag{5} $$

where d_0 is the distance of P_c from O_0; φ_d and ζ_d are the desired pan and tilt angles, respectively; also, $\mathbf{c}_{RT}$ is the position vector of the circular path center, O_c, measured in $O_0x_0y_0z_0$, which is writable in explicit form as follows:

$$ \mathbf{c}_{RT} = d_c \begin{pmatrix} \sin \varphi_c \cos \zeta_c \\ -\cos \varphi_c \cos \zeta_c \\ \sin \zeta_c \end{pmatrix} \tag{6} $$

where d_c is the known distance of O_c from O_0, whereas φ_c and ζ_c are the known pan and tilt angles that make the telescope point toward O_c.

The introduction of Formulas (3), (4), and (6) into vector in Equation (5) together with the assumption that $d_0 \approx d_c = d$, which is justified by the fact that in real applications, $r << d$, yields the following system of equations:

$$ \begin{cases} \sin \varphi_d \cos \zeta_d = \sin \varphi_c \cos \zeta_c \\ \cos \varphi_d \cos \zeta_d = \cos \varphi_c \cos \zeta_c + \frac{r}{d} \cos \omega t \\ \sin \zeta_d = \sin \zeta_c + \frac{r}{d} \sin \omega t \end{cases} \tag{7} $$

By considering that the setup of Figure 6 makes $\cos\zeta_d$ always positive, the first two equations of system (7) yield the following explicit formula:

$$ \varphi_d = \mathrm{atan2}\left(\sin \varphi_c \cos \zeta_c,\ \cos \varphi_c \cos \zeta_c + \frac{r}{d} \cos \omega t \right); \tag{8} $$

whereas the third equation of system (7) results in the following:

$$ \zeta_d = \arcsin\left(\sin \zeta_c + \frac{r}{d} \sin \omega t \right). \tag{9} $$

Equations (8) and (9) provide the values of φ_d and ζ_d as functions of exciting frequency and time that exit, as outputs, from the target block (see Figure 4) and that enter, as inputs, into the inverse-kinematics block.

3. Results

The above-defined virtual experiment was implemented on the built digital twin of the studied RTS by assigning the following values to the experimental setup constants: d = 10 m, r = 0.01 m, φ_c = 30° (0.5236 rad), and ζ_c = 40° (0.6981 rad).

3.1. Implementation of Steps II, III, and IV of the Virtual Experiment Campaign

The experiment starts with the telescope randomly oriented and the target point, P_c, which is at rest. When the target appears, the RTS starts working to collimate the telescope axis with the static target. This collimation phase usually lasts less than 1 s. So, the circular motion of the target point, P_c, is triggered with a fixed delay of 1 s after the target's appearance to be sure that it takes place after the static collimation.

Since having good dynamic performances up to 10 Hz is the design requirement, the values of the control system's parameters have been adjusted by performing a number of tracking experiments in which the motion frequency, f (Equation (2)), of the target is exactly equal to 10 Hz.

The trial-and-error tuning of the PID controller was conducted by sequentially implementing the following steps with the aim of finding the best compromise between the minimum time response and the minimum overshoot. Firstly, the proportional gain, K_p, is adjusted by increasing it until the output signal reaches a critical damping (i.e., just before the oscillation starts). Then, the integration gain, K_i, is added to the previously determined proportional gain and it is tuned by trying to minimize (possibly to zero) the static error. Finally, the fine-tuning is performed by adding and adjusting the derivative gain, K_d, together with the derivative filter time, T_f, with the goal of minimizing the overshoot.

This experimental optimization phase brought to determine the values of the PID controller's parameters (see Equation (1)) reported in Table 1. In addition, for the values of the DC motors' parameters (Figure 5), the methodology proposed in [21], by taking into account the DC motors available on the market, brought to determine the values reported in Table 2.

Table 1. Parameters of each 2-DOF PID controller.

Parameter	*Value*
K_p	20
K_i	2000 s^{-1}
K_d	0.2 s
T_f	100 s

Table 2. DC motor parameters.

Parameter	*Value*
K_m	2.3 Nm/A
K_e	2.3 V/(rad/s)
J	0.068 kg·m^2
B	0.008 Nm/(rad/s)
L_a	0.00261 H
R_a	2.61 Ω

The performances at 10 Hz of the sized RTS are reported in Figures 7–10. In particular, Figures 7 and 8 show the time histories of the pan angle and of the error, $\varphi_d - \varphi$, on the pan angle during tracking, respectively. In Figure 7, the red curve is the time history of the desired pan angle, φ_d (i.e., the one computed using Equation (8)), whereas the blue curve is the time history of the actual pan angle, φ, of the RTS. Moreover, Figures 9 and 10 show the time histories of the tilt angle and of the error, $\zeta_d - \zeta$, on the tilt angle during tracking, respectively. In Figure 9, the red curve is the time history of the desired tilt angle, ζ_d (i.e., the one computed using Equation (9)), whereas the blue curve is the time history of the actual tilt angle, ζ, of the RTS.

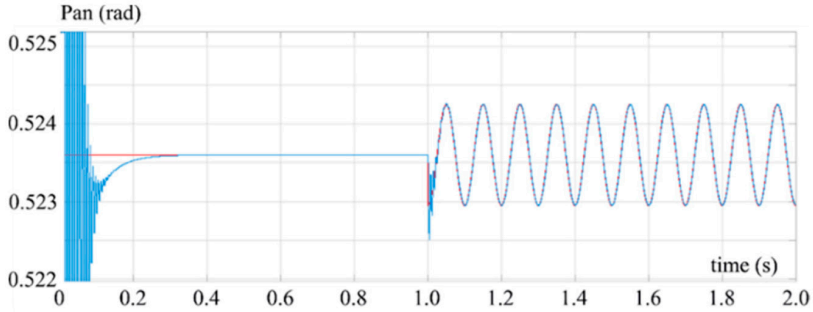

Figure 7. Tracking performance at 10 Hz of an RTS sized with the parameters of Tables 1 and 2: the red curve is the time history of the desired pan angle, φ_d (i.e., the one computed using Equation (8)), whereas the blue curve is the time history of the actual pan angle, φ, of the RTS.

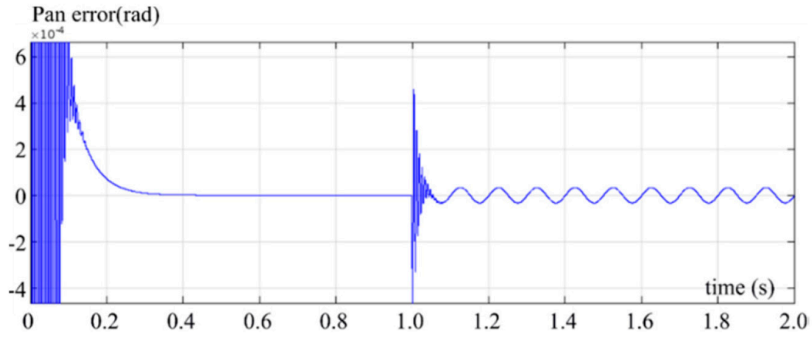

Figure 8. Tracking performance at 10 Hz of an RTS sized with the parameters of Tables 1 and 2: time history of the pan error, $\varphi_d - \varphi$.

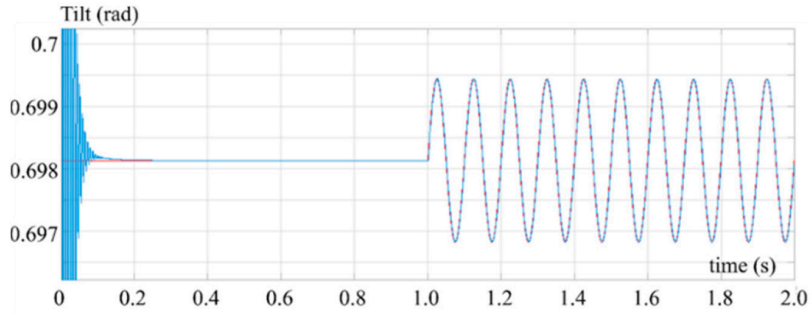

Figure 9. Tracking performance at 10 Hz of an RTS sized with the parameters of Tables 1 and 2: the red curve is the time history of the desired tilt angle, ζ_d (i.e., the one computed using Equation (9)), whereas the blue curve is the time history of the actual tilt angle, ζ, of the RTS.

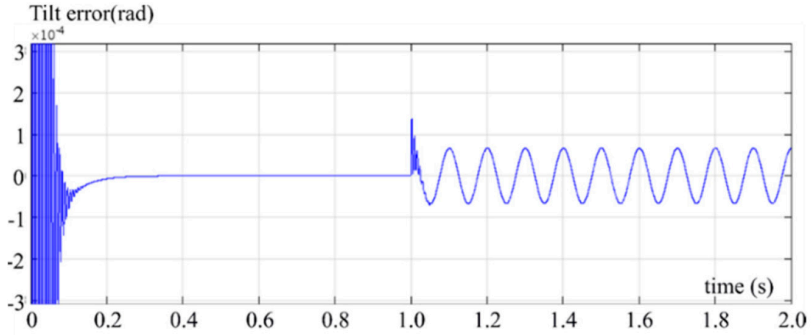

Figure 10. Tracking performance at 10 Hz of an RTS sized with the parameters of Tables 1 and 2: time history of the tilt error, $\zeta_d - \zeta$.

The analysis of these figures reveals that a fraction of a second is sufficient to make the telescope collimate the target point (see Figures 7 and 9). Also, it shows that the maximum tracking error on the pan angle (see Figure 8) is less than 3.5×10^{-5} rad and that the maximum tracking error on the tilt angle (see Figure 10) is less than 7×10^{-5} rad. Such results are satisfactory; as a consequence, the remaining steps of the above-defined procedure can be implemented on the mechatronic system sized using the values of Tables 1 and 2.

3.2. Implementation of the Remaining Steps of the Virtual Experiment Campaign

In order to assess the design results (i.e., the values of Tables 1 and 2) obtained in the previous subsection, the frequency response of the RTS must be determined to verify whether the RTS behavior is still good at frequencies different from 10 Hz.

As explained above (steps (V) and (VI)), the RTS frequency response can be determined by repeating the ad hoc virtual experiment for different frequencies uniformly distributed in an ample range of frequencies. Indeed, if the control system's parameters are not changed and the experiment is repeated with different motion frequencies, the gain and the phase delay between the output and the input can be computed for different frequency values and plotted into diagrams as functions of the target's motion frequency.

Figure 11 shows the obtained Bode plot of the RTS's frequency response. The graphs of Figure 11 hold for both the pan and the tilt angles. In Figure 11, A_i and A_o are the maximum amplitudes of the oscillating input and output, respectively.

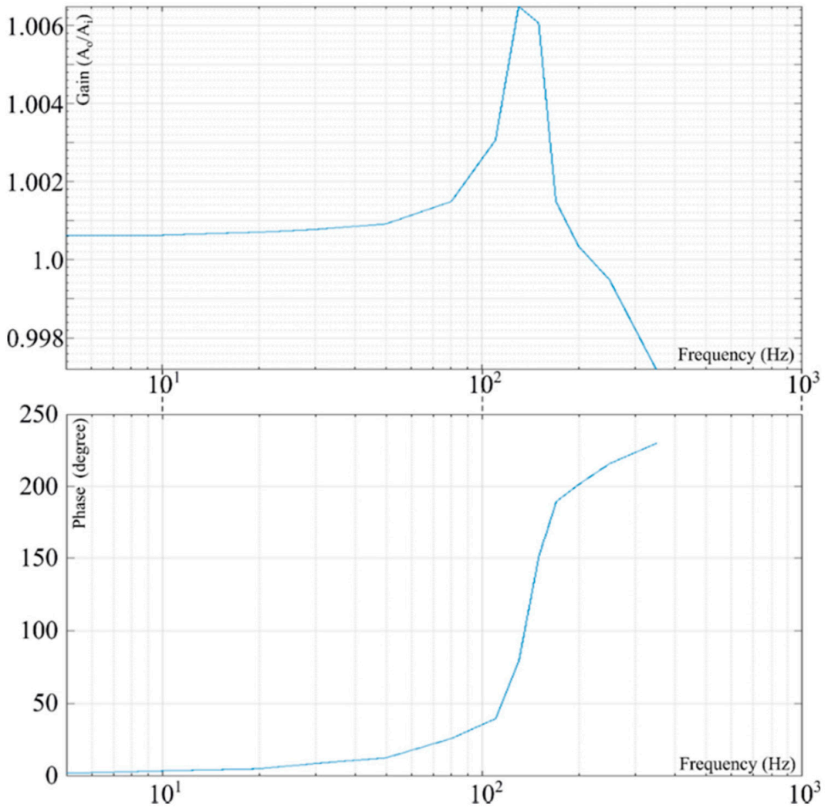

Figure 11. Bode plot of the RTS's frequency response obtained by implementing steps (V) and (VI) (A_i and A_o are the maximum amplitudes of the oscillating input and output; these graphs are valid both for pan and tilt angles).

The analysis of Figure 11 reveals that there is a resonance at 110 Hz with a peak of 1.0062 and that the RTS's tracking performance is good (i.e., it exhibits a practically unitary gain and a negligible delay) in the bandwidth of [0, 10] Hz and it is acceptable (i.e., it still has a practically unitary gain with a phase delay less than 10°) in the bandwidth of [10, 30]

Hz. The conclusion is that the devised design procedure was effective in sizing the control system of the novel RTS architecture so that its tracking frequency limit could be extended up to 10 Hz.

4. Discussion

In the above-described virtual experiment campaign, which was also summarized in [27], the circular path to track does not change either its location (i.e., the O_c coordinates and the plane it lies on) or its shape (i.e., its radius). Even though the chosen location and shape of the path are realistic, what happens when other regions of the RTS workspace are involved needs to be considered as well. Here, this aspect is addressed.

4.1. Sensitivity to the Tracking Path Location

In order to assess this point, the almost-hemispherical workspace (i.e., with a pan rotation, φ, of $[0°, 360]$ and a tilt rotation, ζ, of $[-20°, 100°]$) of the studied RTS has been discretized into a sufficiently high number of telescope–axis directions that are uniformly distributed. The variation ranges of both the pan, φ, and tilt, ζ, angles have been discretized with the following discretization step: $\Delta\varphi = \Delta\zeta = 20°$. Then, along each direction selected through the above-mentioned discretization, a circular path with radius, r, equal to 0.01 m is located (see Figures 6 and 12) so that its center, O_c, is at a distance, d, of 10 m from O_0, and the plane of the circle is perpendicular to the line passing through points O_0 and O_c (Figure 12). The values of the parameters r and d are kept unchanged with respect to the previous virtual experiments to make the results comparable.

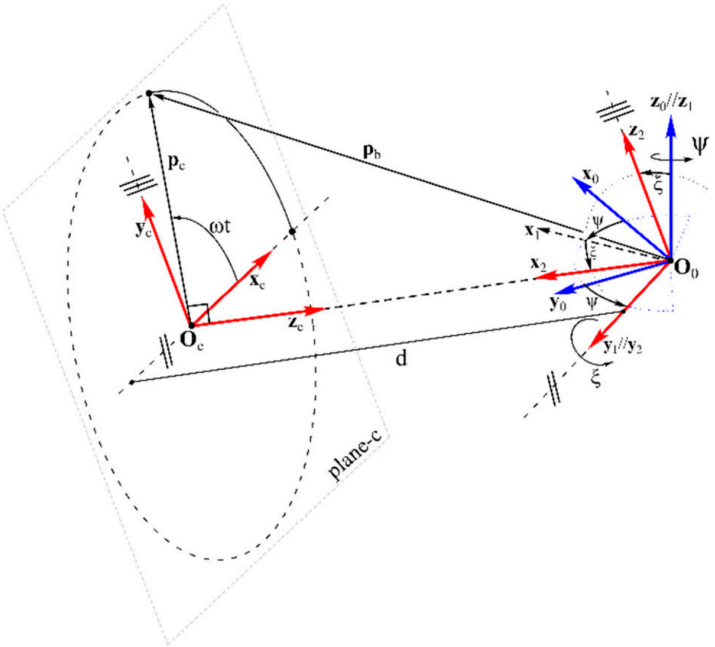

Figure 12. Location of the circular path along one direction selected by discretizing the RTS workspace.

In this case, the virtual experiment campaign consists in repeating tracking tests, in which a target point moves along a circular path identified by the location of point O_c at a constant velocity that corresponds to a motion frequency of 10 Hz (see Equation (2)), for different positions of point O_c.

Now, with reference to Figure 12, the orientation of the reference system $O_c x_c y_c z_c$, fixed to the circular path, with respect to the reference system $O_0 x_0 y_0 z_0$, fixed to the RTS's base, is given by the new rotation matrix that follows:

$$ {}^{0}\mathbf{R}_{c} = \begin{bmatrix} \sin\psi & \cos\psi\sin\xi & -\cos\psi\cos\xi \\ -\cos\psi & \sin\psi\sin\xi & -\sin\psi\cos\xi \\ 0 & \cos\xi & \sin\xi \end{bmatrix} \tag{10} $$

where ψ and ξ are related to the pan, φ_c, and the tilt, ζ_c, angles of the circular path center, O_c, by the following relationships: $\varphi_c = \psi + 90^\circ$ and $\zeta_c = -\xi$.

Moreover, the position vector, $\mathbf{c}_{RT}$, of the circular path center, O_c, measured in $O_0x_0y_0z_0$, has the following explicit form:

$$ \mathbf{c}_{RT} = d\begin{pmatrix} \cos\psi\cos\xi \\ \sin\psi\cos\xi \\ -\sin\xi \end{pmatrix}; \tag{11} $$

and the position vector, $\mathbf{p}_b$ (see Figure 12), of the mobile point, P_c, to track along the circular path, measured in $O_0x_0y_0z_0$, has the following explicit form:

$$ \mathbf{p}_b = d_0\begin{pmatrix} \sin\varphi_d\cos\zeta_d \\ -\cos\varphi_d\cos\zeta_d \\ \sin\zeta_d \end{pmatrix}; \tag{12} $$

where $d_0 = \sqrt{d^2 + r^2}$.

Eventually, the introduction of Formulas (4), (10), (11), and (12) into the relationship $\mathbf{p}_b = \mathbf{c}_{RT} + {}^{0}\mathbf{R}_c\mathbf{p}_c$ (Equation (5)) yields the following new system to solve, which replaces system (7):

$$ \begin{cases} d_0\sin\varphi_d\cos\zeta_d = d\cos\psi\cos\xi + r(\sin\psi\cos\omega t + \cos\psi\sin\xi\sin\omega t) \\ -d_0\cos\varphi_d\cos\zeta_d = d\sin\psi\cos\xi + r(\sin\psi\sin\xi\sin\omega t - \cos\psi\cos\omega t) \\ d_0\sin\zeta_d = -d\sin\xi + r\cos\xi\sin\omega t \end{cases} \tag{13} $$

The new explicit expressions of the desired values of φ_d and ζ_d as functions of the exciting frequency and time, which exit, as outputs, from the target block (see Figure 4) and enter, as inputs, into the inverse-kinematics block, are computable by solving system (13) as follows. The first two equations of system (13) yields the following relationships:

$$ \sin\varphi_d = \frac{a}{d_0\cos\zeta_d} \tag{14a} $$

$$ \cos\varphi_d = -\frac{b}{d_0\cos\zeta_d} \tag{14b} $$

with

$$ a = d\cos\psi\cos\xi + r(\sin\psi\cos\omega t + \cos\psi\sin\xi\sin\omega t), $$

$$ b = d\sin\psi\cos\xi + r(\sin\psi\sin\xi\sin\omega t - \cos\psi\cos\omega t). $$

The introduction of Equations (14a) and (14b) into the trigonometric identity $\cos^2\varphi_d + \sin^2\varphi_d = 1$ yields the following relationship:

$$ \cos\zeta_d = \pm\frac{1}{d_0}\sqrt{a^2 + b^2} \tag{15} $$

which, together with the third equation of system (13), yields the following relationship:

$$ \zeta_d = \operatorname{atan2}\left(r\cos\xi\sin\omega t - d\sin\xi,\ \pm\sqrt{a^2 + b^2}\right) \tag{16} $$

Eventually, the back-substitution of Equation (16) into Equations (14a) and (14b) results in the following relationship:

$$\varphi_d = \text{atan2}\left(\frac{a}{\cos\zeta_d}, -\frac{b}{\cos\zeta_d}\right) \tag{17}$$

Equations (16) and (17) replace Equations (9) and (8), respectively, in this new set of virtual experiments.

The results of this new virtual experiment campaign are provided by giving the mean, the maximum, and the RMS values of the pan error, $|\varphi - \varphi_d|$, and of the tilt error, $|\zeta - \zeta_d|$, during tracking for each selected telescope–axis direction by transforming the discretized values into a continuous surface through Bezier surfaces.

Figures 13–15 show the mean, the RMS, and the maximum values of the pan error, $|\varphi - \varphi_d|$, respectively, both in Cartesian and in polar coordinates. The analysis of these three figures reveals that the pan error is always lower than 10^{-4} rad (=0.00573°) in the whole workspace, which is acceptable for tracking tasks of measurement devices.

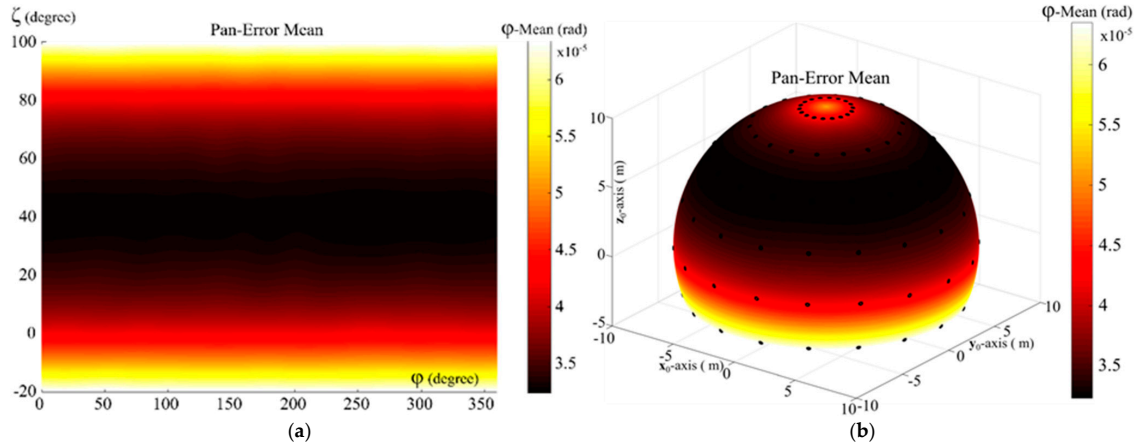

Figure 13. Mean values of the pan error $|\varphi - \varphi_d|$ as a function of the circular path location in the RTS workspace: (**a**) bi-dimensional Cartesian diagram (the coordinates φ and ζ refer to the center, O_c, of the circular path to track), (**b**) polar diagram (the black dots on the hemisphere, centered at O_0, with radius of 10 m, indicate the selected discretized positions of O_c in $O_0x_0y_0z_0$ and, at the same time, the discretized directions of the telescope axis).

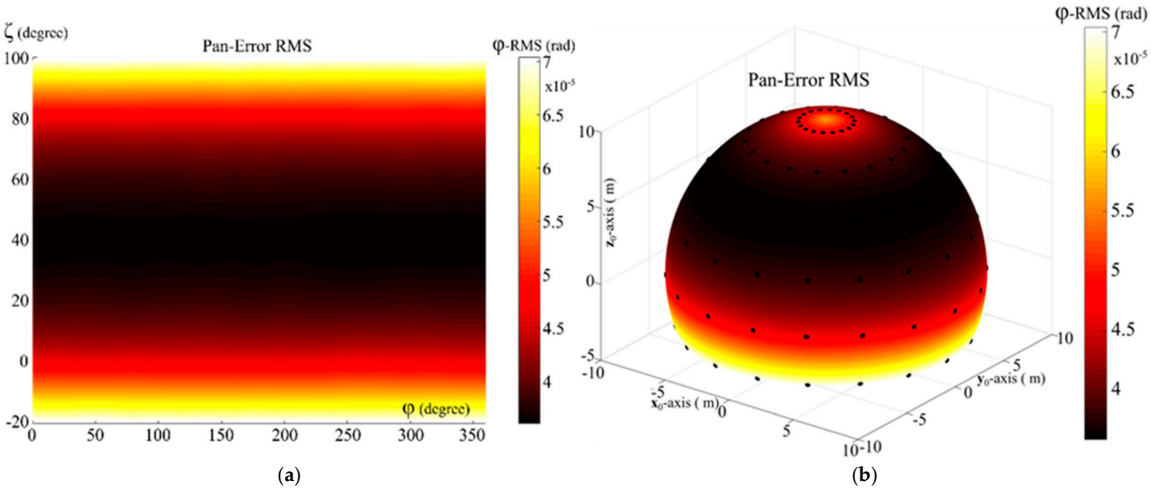

Figure 14. RMS values of the pan error $|\varphi - \varphi_d|$ as a function of the circular path location in the RTS workspace: (**a**) bi-dimensional Cartesian diagram (the coordinates φ and ζ refer to the center, O_c, of the circular path to track), (**b**) polar diagram (the black dots on the hemisphere, centered at O_0, with radius of 10 m, indicate the selected discretized positions of O_c in $O_0x_0y_0z_0$ and, at the same time, the discretized directions of the telescope axis).

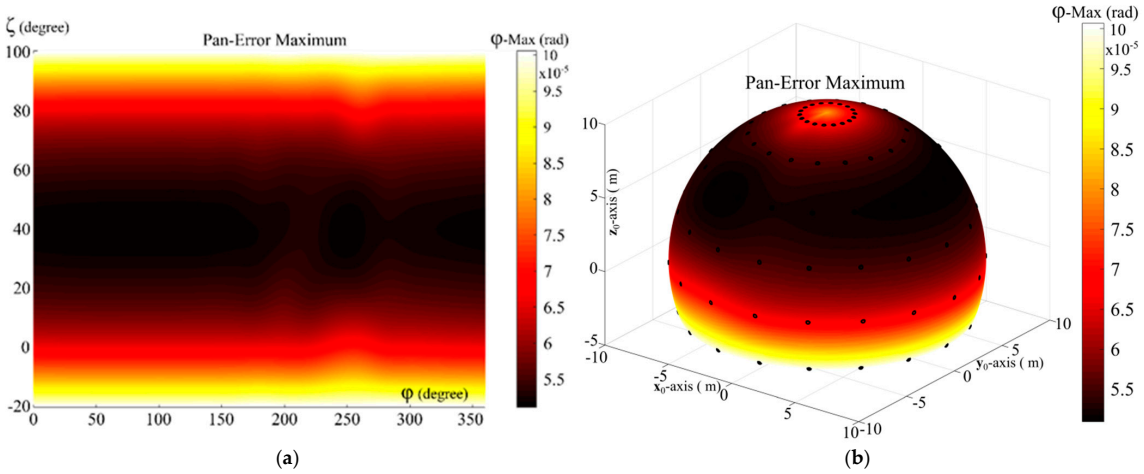

Figure 15. Maximum values of the pan error $|\varphi - \varphi_d|$ as a function of the circular path location in the RTS workspace: (**a**) bi-dimensional Cartesian diagram (the coordinates φ and ζ refer to the center, O_c, of the circular path to track), (**b**) polar diagram (the black dots on the hemisphere, centered at O_0, with radius of 10 m, indicate the selected discretized positions of O_c in $O_0x_0y_0z_0$ and, at the same time, the discretized directions of the telescope axis).

Figures 16–18 show the mean, the RMS, and the maximum values of the tilt error, $|\zeta - \zeta_d|$, respectively, both in Cartesian and in polar coordinates. The analysis of these other three figures reveals that the tilt error is always lower than 0.0000545 rad (=0.00312°) in the whole workspace, which is acceptable for tracking tasks of measurement devices.

The conclusion is that the proposed RTS has good tracking performances up to 10 Hz in all the regions of its workspace.

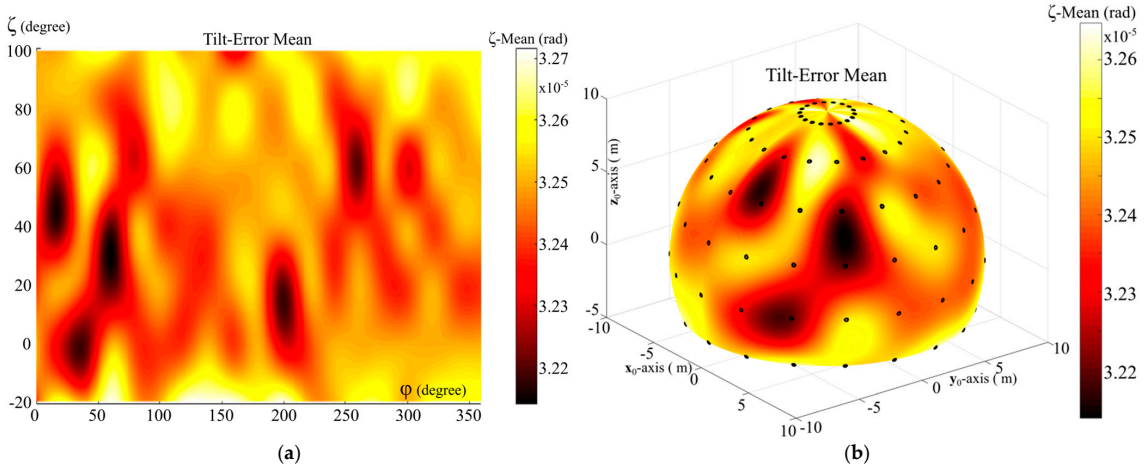

Figure 16. Mean values of the tilt error $|\zeta - \zeta_d|$ as a function of the circular path location in the RTS workspace: (**a**) bi-dimensional Cartesian diagram (the coordinates φ and ζ refer to the center, O_c, of the circular path to track), (**b**) polar diagram (the black dots on the hemisphere, centered at O_0, with radius of 10 m, indicate the selected discretized positions of O_c in $O_0x_0y_0z_0$ and, at the same time, the discretized directions of the telescope axis).

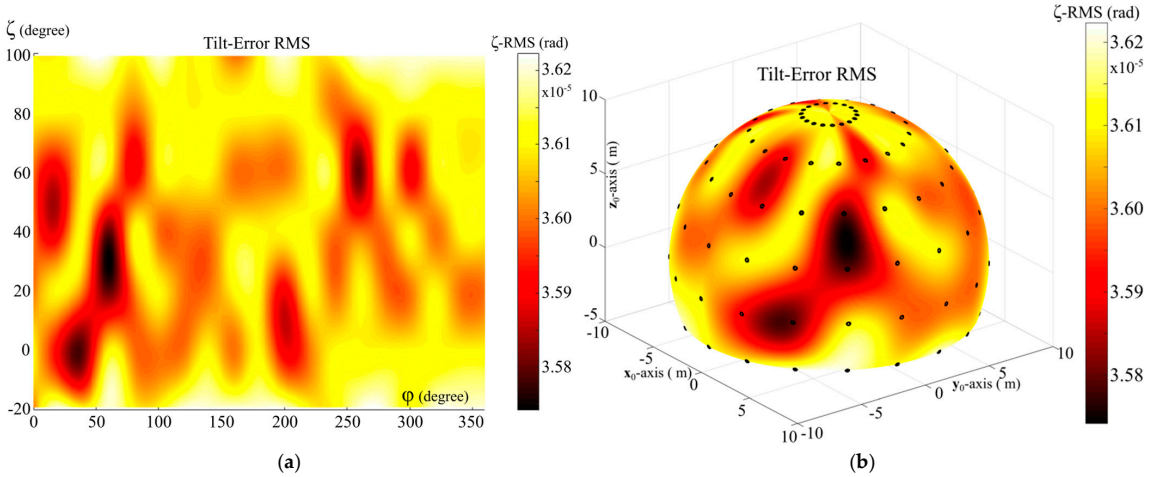

Figure 17. RMS values of the tilt error $|\zeta - \zeta_d|$ as a function of the circular path location in the RTS workspace: (**a**) bi-dimensional Cartesian diagram (the coordinates φ and ζ refer to the center, O_c, of the circular path to track), (**b**) polar diagram (the black dots on the hemisphere, centered at O_0, with radius of 10 m, indicate the selected discretized positions of O_c in $O_0x_0y_0z_0$ and, at the same time, the discretized directions of the telescope axis).

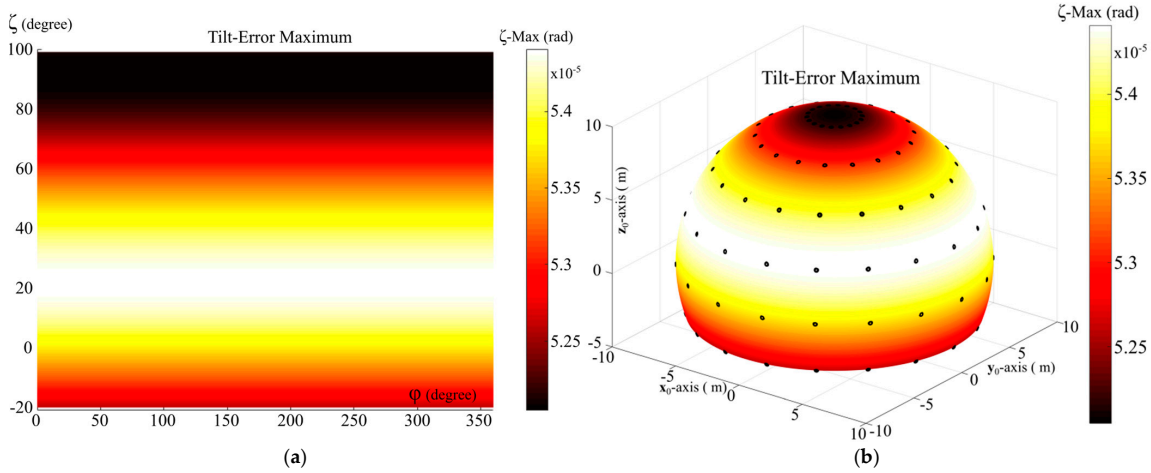

Figure 18. Maximum values of the tilt error $|\zeta - \zeta_d|$ as a function of the circular path location in the RTS workspace: (**a**) bi-dimensional Cartesian diagram (the coordinates φ and ζ refer to the center, O_c, of the circular path to track), (**b**) polar diagram (the black dots on the hemisphere, centered at O_0, with radius of 10 m, indicate the selected discretized positions of O_c in $O_0x_0y_0z_0$ and, at the same time, the discretized directions of the telescope axis).

4.2. 3D-Printed Prototype of the Designed RTS

Based on the above-reported results of the virtual experiment campaigns, a 3D-printed prototype was built and tested. Figure 19 shows some photos of the prototype. Since the mass distribution of such a prototype is different from the one of a real RTS (i.e., the one used in the virtual experiment campaigns), it will have different dynamic performances and cannot be used to verify the above-reported results obtained through the virtual experiment campaigns. Nevertheless, it can be used for functional tests and for checking the effectiveness of the control system board in controlling the DC motors. These tests were conducted and a video is included in this paper's Supplementary Materials, which shows a number of motion tasks implemented using this prototype. The results of these motion tasks confirm the effectiveness of the adopted design methodology.

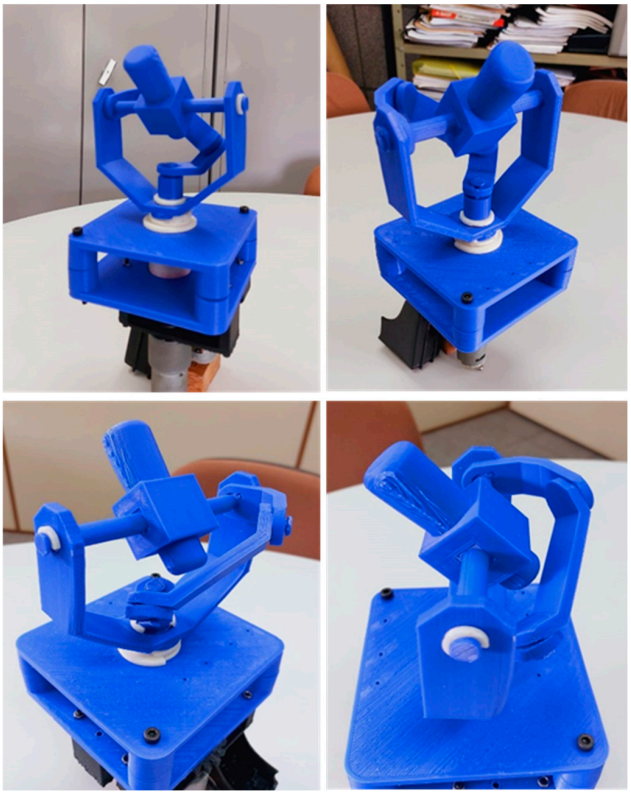

Figure 19. Prototype built by using the results of the proposed design methodology based on ad hoc virtual experiments: photos taken from different points of view.

5. Conclusions

The design of an innovative robotic total station (RTS) was completed by sizing its control system so that it can track a mobile target up to 10 Hz. The tracking performances of the sized RTS were checked in all the regions of its workspace. This check revealed that the collimation error of the RTS during tracking is always lower than 0.006°, which is acceptable for tracking tasks of measurement devices.

The adopted design methodology is based on the RTS's digital twin and on ad hoc virtual experiments. This methodology is applicable to the design of other mechatronic systems; moreover, the proposed ad hoc virtual experiments can also be used to design other pointing systems.

A 3D-printed prototype of the studied RTS was built and used for functional tests and to check the effectiveness of the designed control system. Both these tests and checks confirm the effectiveness of the proposed design methodology.

Supplementary Materials: The following supporting information can be downloaded at: https://www.mdpi.com/article/10.3390/electronics13214248/s1. One video showing a number of motion tasks of the built prototype.

Author Contributions: Conceptualization, H.S., R.D.G. and R.S.; methodology, R.D.G.; software, H.S. and R.S.; validation, H.S., R.D.G. and R.S.; formal analysis, H.S., R.D.G. and R.S.; investigation, H.S., R.D.G. and R.S.; resources, H.S., R.D.G. and R.S.; data curation, H.S., R.D.G. and R.S.; writing—original draft preparation, H.S., R.D.G. and R.S.; writing—review and editing, H.S., R.D.G. and R.S.; supervision, R.D.G.; project administration, H.S. and R.D.G.; funding acquisition, H.S. and R.D.G. All authors have read and agreed to the published version of the manuscript.

Funding: This work was developed at the Laboratory of Mechatronics and Virtual Prototyping (LaMaViP) of Ferrara Technopole, supported by UNIFE–University of Ferrara—Project UNIFE FIRD2023, in partnership with the Laboratory of Applied Robotics of Federal University of Santa

Catarina, supported by CNPq—Conselho Nacional de Desenvolvimento Científico e Tecnológico (National Council for Scientific and Technological Development) Project 307249/2021-2, Brazil.

Data Availability Statement: The original contributions presented in the study are included in the article/Supplementary Materials; further inquiries can be directed to the authors.

Acknowledgments: The authors would like to acknowledge Luan Meneghini for his support in building the prototype.

Conflicts of Interest: The authors declare no conflicts of interest. The funders had no role in the design of the study; in the collection, analyses, or interpretation of data; in the writing of the manuscript; or in the decision to publish the results.

References

1. Nadolinets, L.; Levin, E.; Akhmedov, D. *Surveying Instruments and Technology*; CRC Press: Boca Raton, FL, USA, 2017; ISBN 978-1-4987-6238-0.
2. Kirschner, H.; Stempfhuber, W. The Kinematic Potential of Modern Tracking Total Stations—A State of the Art Report on the Leica TPS 12001. In Proceedings of the 1st International Conference on Machine Control & Guidance, Zurich, Switzerland, 24–26 June 2008; Ingensand, H., Stempfhuber, W., Eds.; Eidgenössische Technische Hochschule (ETH): Zurich, Switzerland, 2008; pp. 51–60.
3. Kleemaier, G.; Maar, H.; Zogg, H.M. Enhanced Automation Performance of Total Stations for Kinematic Applications Using the ATR Plus Technology. In Proceedings of the 5th International Conference on Machine Control and Guidance, Vichy, France, 5–6 October 2016.
4. Brownjohn, J.M.W.; Koo, K.Y.; Scullion, A.; List, D. Operational deformations in long-span bridges. *Struct. Infrastruct. Eng.* **2015**, *11*, 556–574. [CrossRef]
5. Psimoulis, P.; Peppa, I.; Bonenberg, L.; Ince, S.; Meng, X. Combination of GPS and RTS Measurements for the Monitoring of Semi-Static and Dynamic Motion of Pedestrian Bridge. In Proceedings of the 3rd Joint International Symposium on Deformation Monitoring, Vienna, Austria, 30 March–1 April 2016.
6. Lienhart, W.; Ehrhart, M.; Grick, M. High frequent total station measurements for the monitoring of bridge vibrations. *J. Appl. Geod.* **2017**, *11*, 1–8. [CrossRef]
7. Yu, J.; Zhu, P.; Xu, B.; Meng, X. Experimental Assessment of High Sampling-Rate Robotic Total Station for Monitoring Bridge Dynamic Responses. *Measurement* **2017**, *104*, 60–69. [CrossRef]
8. Psimoulis, P.; Stiros, S. Measuring Deflections of a Short-Span Railway Bridge Using a Robotic Total Station. *J. Bridge Eng.* **2013**, *18*, 182–185. [CrossRef]
9. Moschas, F.; Stiros, S. Rapid Decay of a Timber Footbridge and Changes in Its Modal Frequencies Derived from Multiannual Lateral Deflection Measurements. *J. Bridge Eng.* **2014**, *19*, 05014005.
10. Psimoulis, P.; Stiros, S. A Supervised Learning Computer-Based Algorithm to Derive the Amplitude of Oscillations of Structures Using Noisy GPS and Robotic Theodolites (RTS) Records. *Comput. Struct.* **2012**, *92–93*, 337–348. [CrossRef]
11. Charalampous, E.; Psimoulis, P.; Guillaume, S.; Spiridonakos, M.; Klis, R.; Bürki, B.; Rothacher, M.; Chatzi, E.; Luchsinger, R.; Feltrinet, G. Measuring Sub-mm Structural Displacements Using QDaedalus: A Digital Clip-On Measuring System Developed for Total Stations. *Appl. Geomat.* **2015**, *7*, 91–101. [CrossRef]
12. Gatti, M. Measurement of vibration frequencies of ties in masonry arches by means of a robotic total station. *Earthq. Eng. Eng. Vib.* **2022**, *21*, 489–500. [CrossRef]
13. Simas, H.; Di Gregorio, R.; Simoni, R.; Gatti, M. Parallel Pointing Systems Suitable for Robotic Total Stations: Selection, Dimensional Synthesis, and Accuracy Analysis. *Machines* **2024**, *12*, 54. [CrossRef]
14. Hervé, J.M. Uncoupled actuation of pan-tilt wrists. *IEEE Trans. Robot.* **2006**, *22*, 56–64. [CrossRef]
15. Li, Q.; Hervé, J.M.; Ye, W. *Geometric Method for Type Synthesis of Parallel Manipulators*; Springer: Singapore, 2020; ISBN 978-981-13-8754-8. [CrossRef]
16. Gogu, G. *Structural Synthesis of Parallel Robots*; Springer: Dordrecht, The Netherlands, 2014; Volume 1–5.
17. Das, S. *Modeling and Simulation of Mechatronic Systems Using Simscape*; Springer: Cham, Switzerland, 2020; ISBN 978-3-031-79652-4. [CrossRef]
18. Russel, K.; Shen, J.Q.; Sodhi, R.S. *Kinematics and Dynamics of Mechanical Systems: Implementation in MATLAB and Simscape Multibody*, 3rd ed.; CRC Press: Boca Raton, FL, USA, 2023; ISBN 9781032328324. [CrossRef]
19. Rehman, A.U.; Khan, M.U.; Rehman, M.T.; Shehzad, W.; Zaman, S.; Khan, M.W. Mathematical Modelling and Implementation of 2DOF Standard, Parallel & Series PID Controllers. In Proceedings of the 2021 6th International Multi-Topic ICT Conference (IMTIC), Jamshoro & Karachi, Pakistan, 10–12 November 2021.
20. Sahu, R.K.; Panda, S.; Rout, U.K.; Sahoo, D.K. Teaching learning based optimization algorithm for automatic generation control of power system using 2-DOF PID controller. *Int. J. Electr. Power Energy Syst.* **2021**, *77*, 287–301. [CrossRef]
21. Aslam, S.; Hannan, S.; Sajjad, U.; Zafar, W. Implementation of PID on PIC24F series microcontroller for speed control of a DC motor using MPLAB and Proteus. *Adv. Sci. Technol. Res. J.* **2016**, *10*, 40–50. [CrossRef] [PubMed]

22. Visioli, A.; Legnani, G. On the trajectory tracking control of industrial SCARA robot manipulators. *IEEE Trans. Ind. Electron.* **2002**, *49*, 224–232. [CrossRef]
23. Yuan, M.; Manzie, C.; Good, M.; Shames, I.; Gan, L.; Keynejad, F.; Robinette, T. A review of industrial tracking control algorithms. *Control Eng. Pract.* **2020**, *102*, 104536. [CrossRef]
24. Bansal, H.O.; Sharma, R.; Shreeraman, P.R. PID Controller Tuning Techniques: A Review. *J. Control Eng. Technol.* **2012**, *2*, 168–176.
25. Somefun, O.A.; Akingbade, K.; Dahunsi, F. The dilemma of PID tuning. *Annu. Rev. Control* **2021**, *52*, 65–74. [CrossRef]
26. Borase, R.P.; Maghade, D.K.; Sondkar, S.Y.; Pawar, S.N. A review of PID control, tuning methods and applications. *Int. J. Dynam. Control* **2021**, *9*, 818–827. [CrossRef]
27. Simas, H.; Di Gregorio, R.; Simoni, R. Dynamic Design of a Fast Robotic Total Station Based on Ad-Hoc-Conceived Virtual Experiments Implemented through a Digital Twin. In Proceedings of the IEEE/ASME MESA 2024—20th International Conference on Mechatronic, Embedded Systems and Applications, Genova, Italy, 2–4 September 2024. Paper No. 55.